Experimental Investigation of Early-Age Cracking Behavior in Concrete Slabs Reinforced

Mr. Chandrahas B. Patil[1], Dr. Irfan Kalal[2], Dr. Prashant Bamane[3]

[1]Research Scholar, Civil Engineering Department, Shri Jagdish Prasad Jhabarmal Tibrewala University, Vidyanagari, Jhunjhunu, Rajasthan, India

[2]Assisitant Professor, Civil Engineering Department, Shri Jagdish Prasad Jhabarmal Tibrewala University, Vidyanagari, Jhunjhunu, Rajasthan, India

[3]Associate Professor, Civil Engineering Department, SVERI's College of Engineering, Pandharpur

*** Corresponding Author:** *Mr. Chandrahas B. Patil*

Abstract-

This study presents an integrated experimental and numerical analysis of cracking in concrete slabs reinforced with Glass Fiber Reinforced Polymer (GFRP) bars. The primary focus is on early-age cracking caused by plastic shrinkage, prior to examining the long-term cracking performance over the service life of concrete structures. A key objective is to assess the ability of GFRP reinforcement to limit the formation and propagation of plastic shrinkage cracks. To achieve this, nine small-scale slab specimens were subjected to controlled evaporation conditions, simulating the environmental factors that contribute to early-age cracking. Crack development was monitored periodically through imaging, and measurements of crack widths were recorded. The study included comparisons between slabs reinforced with conventional steel bars, those reinforced with GFRP bars, and unreinforced control specimens. Observations indicate that, during the plastic shrinkage phase, neither the timing of crack initiation nor the subsequent crack openings are significantly affected by the presence of reinforcing bars. To explore the underlying mechanisms, six early-age bond tests were conducted for both steel and GFRP bars at 1, 2, and 3 hours after exposure to the controlled evaporation rate. In parallel, concrete strength evolution and setting times were assessed using penetration resistance tests on representative mortar samples. The numerical component employs a three-dimensional Voronoi cell lattice model, which discretizes relative humidity, temperature, and displacement fields to provide a detailed representation of material behavior under the specified environmental conditions. Using the experimentally measured bond properties, simulations indicate that while reinforcing bars do not entirely prevent plastic shrinkage cracking, they do limit crack widths and moderate crack propagation. These findings highlight the partial effectiveness of GFRP and steel reinforcements in controlling early-age cracking, providing insights into their performance during the critical initial hours of concrete curing.

Keywords -Early-age concrete cracking, Plastic shrinkage ,GFRP reinforcement ,Steel reinforcement, Crack width measurement, Bond behavior, Concrete slab, Voronoi cell lattice model, Numerical simulation.

I.INTRODUCTION

The durability of reinforced concrete is strongly influenced by the corrosion of steel reinforcement, particularly under aggressive environmental conditions. Early-age cracking plays a significant role in promoting corrosion by creating pathways for deleterious agents to reach embedded steel. Controlling crack formation at the initial stages of concrete curing is therefore essential to enhance service life. An alternative approach to mitigate corrosion-related durability issues is the use of non-corroding reinforcement materials. Plastic shrinkage cracking is among the earliest forms of distress in concrete elements. If unaddressed, these cracks can compromise structural durability and longevity. Factors contributing to plastic cracking include water evaporation, bleeding, settlement of solid particles, capillary action, and surface finishing. When the evaporation rate surpasses the rate at which bleed water replenishes the surface, plastic shrinkage cracks

develop. Influencing parameters also include fine aggregate content, water-to-cement ratio, admixtures, member size, and construction practices. Fresh concrete in hot, dry, or windy conditions is especially susceptible, with flat structural elements such as pavements, slabs, bridge decks, and beams being most affected. Restrained shrinkage induces tensile stresses, further promoting crack formation.

This research focuses on the use of glass fiber-reinforced polymer (GFRP) bars as reinforcement for concrete exposed to harsh environments, such as marine conditions. GFRP bars offer corrosion resistance, electromagnetic neutrality, high strength-to-weight ratio, and superior fatigue tolerance, while being significantly lighter than steel, which reduces handling and installation costs. The bond behavior between GFRP and concrete is critical in governing the performance of the composite system. Although FRP reinforcement has been successfully applied in structural members for over three decades, its use as secondary reinforcement to control plastic shrinkage in non-structural concrete members is more recent. Conventional steel reinforcement has limited effectiveness in restricting plastic shrinkage cracks, whereas the bond characteristics and lower stiffness mismatch of GFRP may offer advantages. In this study, the performance of GFRP bars was evaluated relative to conventional steel through combined experimental and numerical approaches. Laboratory experiments showed that the type of reinforcement does not significantly affect the timing or initial width of plastic shrinkage cracks. Numerical modeling, however, indicates that crack opening is influenced by the type of reinforcement, confirming the role of GFRP in moderating crack development while not entirely preventing it.

Objectives

1. To assess the feasibility of replacing Ordinary Portland Cement (OPC) with Ground Granulated Blast Furnace Slag (GGBS) as a sustainable binder in order to minimize greenhouse gas emissions.
2. To evaluate the performance of fiber-reinforced eco-crete mixes prepared with varying mix proportions, with a focus on controlling and reducing early-age cracking.

II.MATERIAL

Concrete

Several concrete mixtures were prepared to promote the likelihood of plastic shrinkage cracking. The mixtures were designed in accordance with ACI 211.1-91 [23]. No chemical admixtures or supplementary cementitious materials were included, and the cement content was intentionally kept high to enhance the potential for plastic shrinkage. Previous studies have shown that increased cement content correlates with higher crack intensity [24].

Type I/II Portland cement was used along with locally sourced fine and coarse aggregates. To further encourage plastic shrinkage, a small No. 89 coarse aggregate was selected [25]. The detailed cement composition and mixture proportions are provided in Table 1 and Table 2, respectively.

To accelerate surface water evaporation, the mixing water was preheated to 50 °C prior to incorporation into the mix. While elevated water temperature can increase bleeding and segregation, the 50 °C target was chosen to achieve the desired balance of bleed water, slump, and compressive strength [26]. Both fine and coarse aggregates were thoroughly dried before use to ensure uniform concrete temperature across all batches and to eliminate additional moisture from the aggregates. Drying the aggregates also contributes to a reduction in bleed water, helping maintain consistency in the mixture behavior.

Table 1. Cement composition.

Property	**CaO**	**SiO_2**	**Al_2O_3**	**Fe_2O_3**	**MgO**	**SO_3**	**Na_2O**	**K_2O**	**Loss on ignition**
wt%	64.1	20.3	4.8	3.5	0.9	2.7	0.12	0.30	2.5

Table 2. Concrete mixture design.

Parameter	Portland Cement Type I/II	Water	Coarse Aggregate #89	Fine Aggregate (Sand)	Unit Weight	w/c
kg/m³	517	291	669	860	2337	0.56
lb/yd³	871	491	1128	1449	3939	–

GFRP and Steel Reinforcement Bars

The study examined three types of slabs. In addition to plain concrete slabs, which acted as control specimens, slabs reinforced with either traditional steel bars or Glass Fiber Reinforced Polymer (GFRP) bars were evaluated. Both reinforcement types had a nominal diameter of 9.5 mm (0.375 in). The steel bars were conventional reinforcement bars with a modulus of elasticity of 200 GPa (29.0 Msi). The detailed physical and mechanical properties of the GFRP bars are provided in Tables 3 and 4.

Table 3: Physical and Mechanical Properties of GFRP Rebar

GFRP Rebar	Bar Designation No.	Fiber Type	Nominal Diameter, mm [in]	Nominal Cross-Sectional Area, mm² [in²]	Measured Cross-Sectional Area, mm² [in²]	Fiber Content, %
	M10 [3]	Glass	9.5 [0.375]	71 [0.11]	87.67 [0.136]	80

Table 4. Mechanical properties of GFRP rebar.

Guaranteed Tensile Strength, MPa [ksi]	Modulus of Elasticity, GPa [Msi]	Mean Ultimate Tensile Strain	Guaranteed Bond Strength, MPa [ksi]
952 [138.1]	60.5 [8.78]	1.9	1.84 [0.27]

The likelihood of plastic shrinkage cracking was evaluated using a modified version of the apparatus described in ASTM C1579-21 [27]. This method employs small slab specimens fitted with metallic inserts secured to the base of the formwork. Each insert consists of a 6.35 mm (0.25 in) steel plate with three welded T-bars, as depicted in Figure 1. The T-bars located at the ends of the insert serve to restrain plastic shrinkage, promoting the development of cracks, whereas the T-bar positioned at mid-span functions as a stress concentrator, influencing the initial location of crack formation. To facilitate shrinkage while minimizing adhesion, the long sides of the mold between the restraints were oiled, whereas the short sides were left untreated to enhance the restraining effect at the ends. Polyester sheets were also placed on the steel baseplate between the mid-span riser and the end restraints to further reduce bonding.

While ASTM C1579-21 primarily addresses testing of fiber-reinforced or plain concrete, in this study, each reinforced specimen contained a reinforcing bar with a 19 mm (0.75 in) concrete cover, as shown in Figure 1a. Evaluating the plastic shrinkage behavior with different bar diameters or concrete covers remains a topic for future research. Additionally, the effect of surface texturing—which is sometimes applied to improve skid resistance or achieve other performance goals—on bleed water movement and subsequent surface drying also warrants further investigation.

A key challenge in this testing methodology is achieving consistent cracking during the early stages of concrete setting. To address this, an environmental chamber was specifically designed and constructed to

create the critical evaporation conditions necessary for plastic shrinkage cracking. Environmental parameters were carefully controlled for the first six hours of testing. Across all slab specimens, the average conditions maintained were a wind speed of 7.8 m/s, relative humidity of 37%, and an ambient temperature of 32.2 °C. Measurements taken at 30-minute intervals indicated average standard deviations of 0.46 m/s for wind speed, 2.60% for relative humidity, and 1.53 °C for temperature. These conditions reliably induced plastic shrinkage cracking in all specimens.

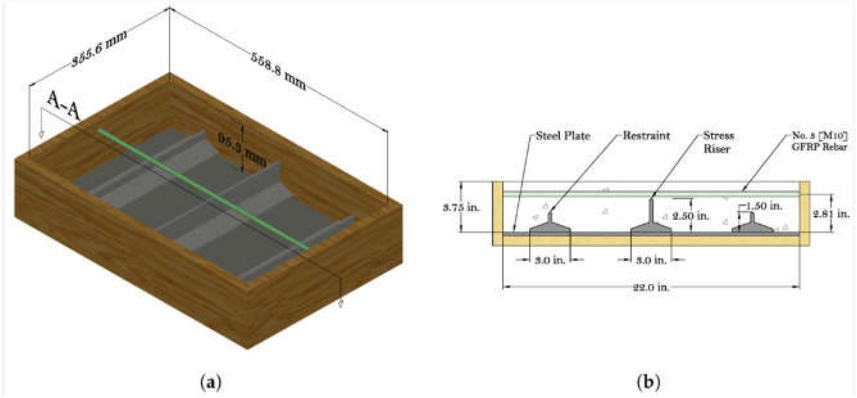

Figure 1. Apparatus for simulating plastic shrinkage cracking: (a) three-dimensional schematic of the setup, and (b) cross-sectional view along section A–A.

Furthermore, crack initiation and propagation were monitored by capturing images of the drying concrete surface. Subsequent image processing provided quantitative information on the timing of crack initiation and the progression of crack widths over time.

Early-Age Bond Test

The early-age bond between reinforcement and concrete was investigated following ASTM D7913-14 [28], as the ability to control crack formation is closely linked to the bond performance of the reinforcement. The configuration of the bond specimens is shown in Figure 2. A total of six samples were prepared in accordance with ASTM D7913-14: three reinforced with GFRP bars and three with steel bars. The specimens were tested after being subjected to the controlled environmental conditions for 1, 2, and 3 hours.

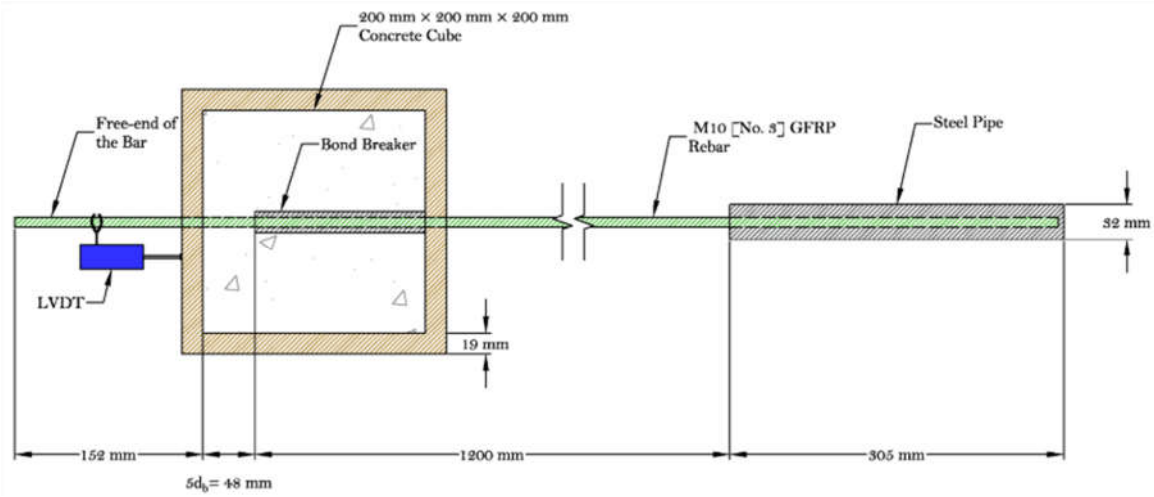

Figure 2. Early-age bond test specimen.

Although elevated curing temperatures can affect the bond behavior of concrete with GFRP reinforcement, the average chamber temperature in this study was 32.2 °C, which is considered low enough to minimize this effect [29]. The same concrete mix used for the plastic shrinkage tests was employed for the bond tests. A companion set of pullout tests was conducted using this mix to quantify the early-age bond characteristics of the GFRP bars.

The pullout tests were performed on a 2000 kN (450 kips) horizontal Universal Testing Machine (UTM) under displacement-controlled loading, applying the load at a rate of 1.3 mm/min (0.050 in/min). A 440 kN (100 kip) load cell recorded the applied load, while a Linear Variable Differential Transformer (LVDT) installed at the free end of the bar measured slip. The overall test setup is illustrated in Figure 3b.

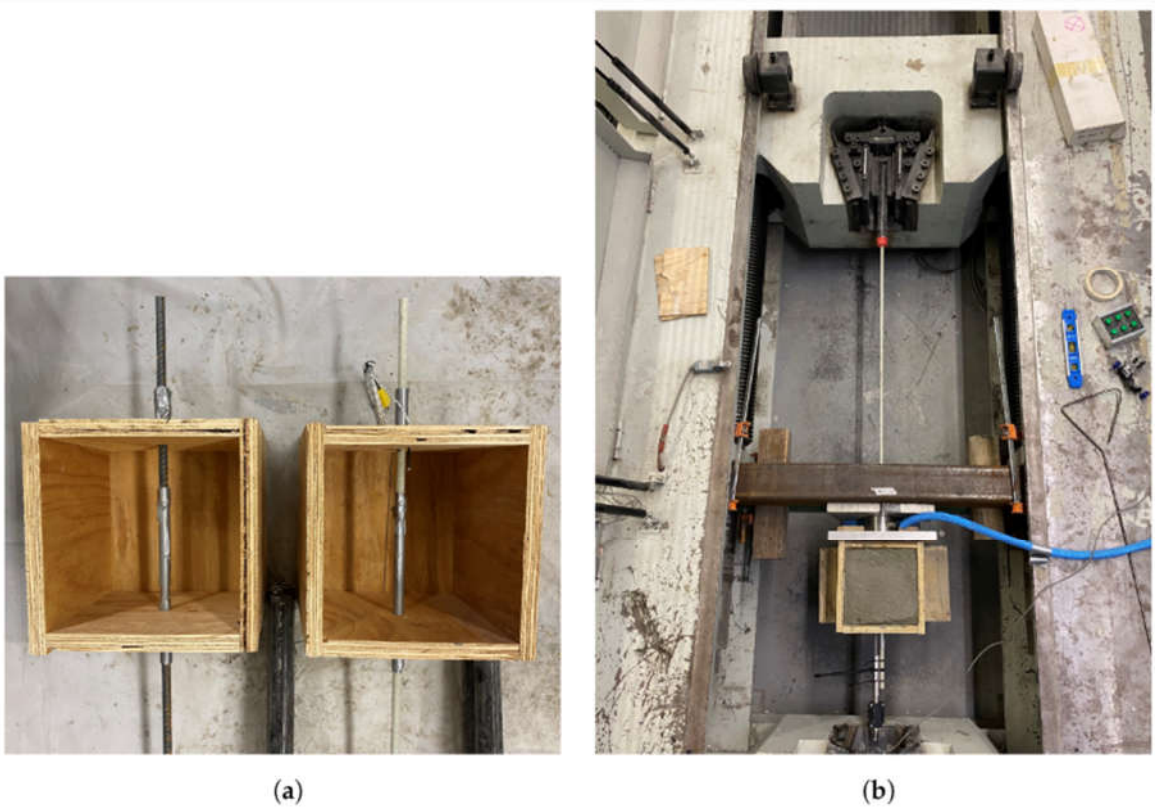

Figure 3. Early-age bond test: (**a**) bond test molds and (**b**) test setup.

Penetration Test

The time of setting and early-age strength development of the concrete were assessed using the ASTM C403-16 [30] Standard Test Method for Time of Setting of Concrete Mixtures by Penetration Resistance. The results obtained from this test were later utilized in the modeling approach presented in this study. Three specimens, each measuring 150 mm × 150 mm × 150 mm (6 in × 6 in × 6 in), were prepared. The concrete mixture was sieved through a 4.75 mm sieve to produce the representative mortar required by ASTM C403-16.

IV. Experimental Results

Plastic Shrinkage Test

Table 5 summarizes the results of the plastic shrinkage tests, including the time of crack initiation, measured crack area and length, and the calculated average crack width after six hours under the specified evaporation conditions. Figure 4 shows a typical concrete specimen immediately after surface finishing and following the development of cracks. Cracks consistently appeared between 113 and 141 minutes after the initial contact of cement with water.

Representative raw and processed images of the central portion of the cracked specimens are presented in Figure 5. Crack area and length were quantified using the ImageJ software for image analysis. The observed crack widths were relatively uniform along the crack lengths and did not significantly decrease near the reinforcement. During this early stage, the bond between concrete and reinforcement is not yet fully developed, resulting in limited stress transfer. Consequently, as anticipated, the reinforcement provided minimal restraint against plastic shrinkage cracking.

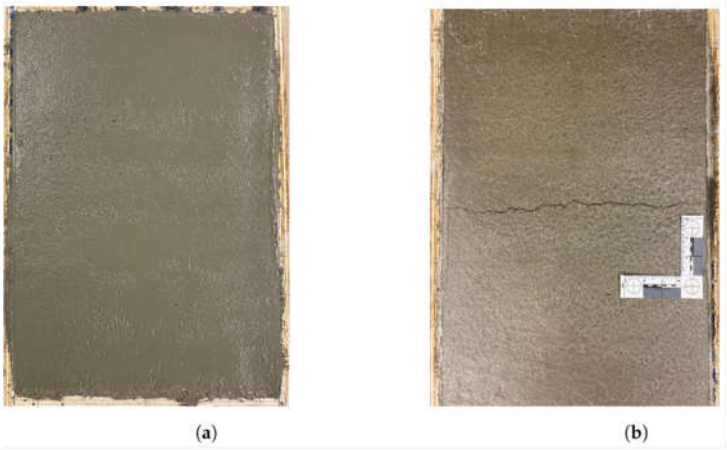

Figure 4. A typical plastic shrinkage specimen: (**a**) after surface finishing and (**b**) after plastic shrinkage cracking.

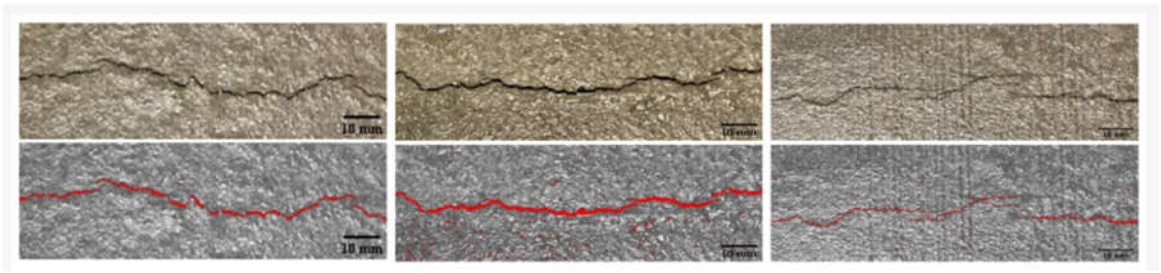

Figure 5. Original (**above**) and postprocessed (**below**) images of cracking of the slab surface above the stress riser; from **left** to **right**: P-SC-1, S-SC-1, G-SC-1.

Table 5. Measured crack data at six hours after concrete casting.

Specimen ID	Reinforcement	Crack Onset (min)	Crack Area, mm² [in²]	Crack Length, mm [in]	Crack Width, mm [in]
P-SC-1	Plain	139	133.5 [0.207]	345.4 [13.6]	0.39 [0.015]
P-SC-2	Plain	132	137.4 [0.213]	290.0 [11.4]	0.47 [0.019]
P-SC-3	Plain	131	202.6 [0.314]	375.8 [14.8]	0.54 [0.021]
S-SC-1	Steel	113	246.5 [0.382]	353.1 [13.9]	0.70 [0.027]
S-SC-2	Steel	141	73.5 [0.114]	188.0 [7.4]	0.39 [0.015]
S-SC-3	Steel	131	129.7 [0.201]	342.9 [13.5]	0.38 [0.015]

G-SC-1	GFRP	115	112.9 [0.175]	340.4 [13.4]	0.33 [0.013]
G-SC-2	GFRP	NA	58.1 [0.090]	139.7 [5.5]	0.42 [0.016]
G-SC-3	GFRP	120	219.4 [0.340]	322.6 [12.7]	0.68 [0.027]

A control specimen composed of plain concrete was cast and cured under laboratory conditions for 18 hours. No visible cracking was observed in this specimen (Figure 6d). This outcome demonstrates that plastic shrinkage cracking can be effectively avoided when adequate curing practices are implemented to maintain moisture at the concrete surface and when casting is performed under environmental conditions where the evaporation rate does not reach critical levels.

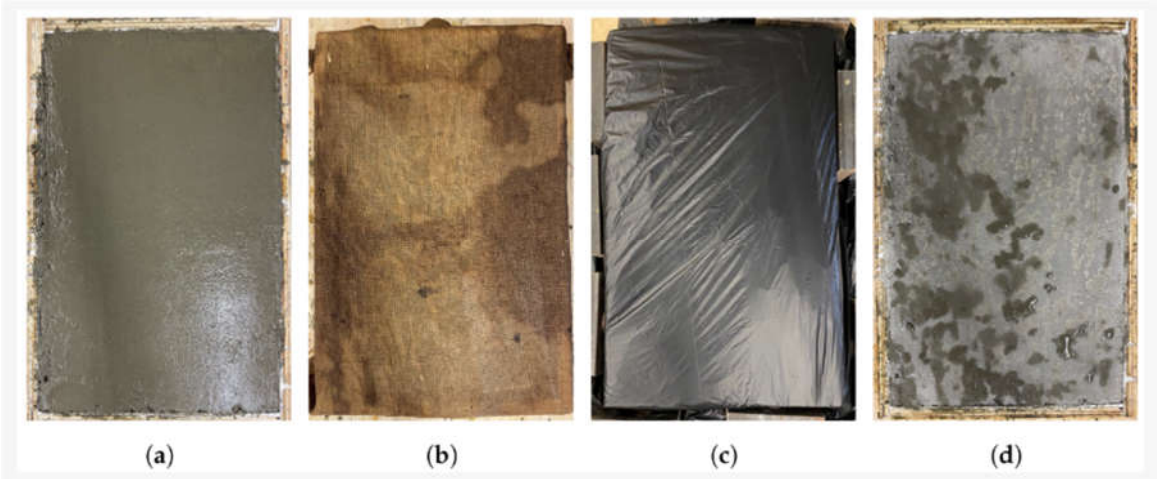

Figure 6. Cured specimen: (**a**) after casting, (**b**) with wet burlap, (**c**) under plastic, and (**d**) after 18 h curing.

Figure 7a presents the temperature evolution of all nine concrete specimens, recorded using thermocouples embedded 51 mm (2 in) beneath the concrete surface. The average air temperature inside the environmental chamber is also shown for reference. As illustrated in Figure 7a, crack initiation occurred when the concrete temperature ranged approximately between 24 and 28 °C (75 to 81 °F). For most specimens, a reduction in temperature was observed shortly after casting, which is attributed to evaporative cooling effects, as discussed later. To examine temperature gradients through the concrete depth, specimen P-SC-2 was instrumented with an additional thermocouple positioned 13 mm (0.5 in) below the surface. The results shown in Figure 7b indicate that temperature decreases toward the surface, primarily due to combined evaporative and convective heat transfer between the concrete and the surrounding environment.

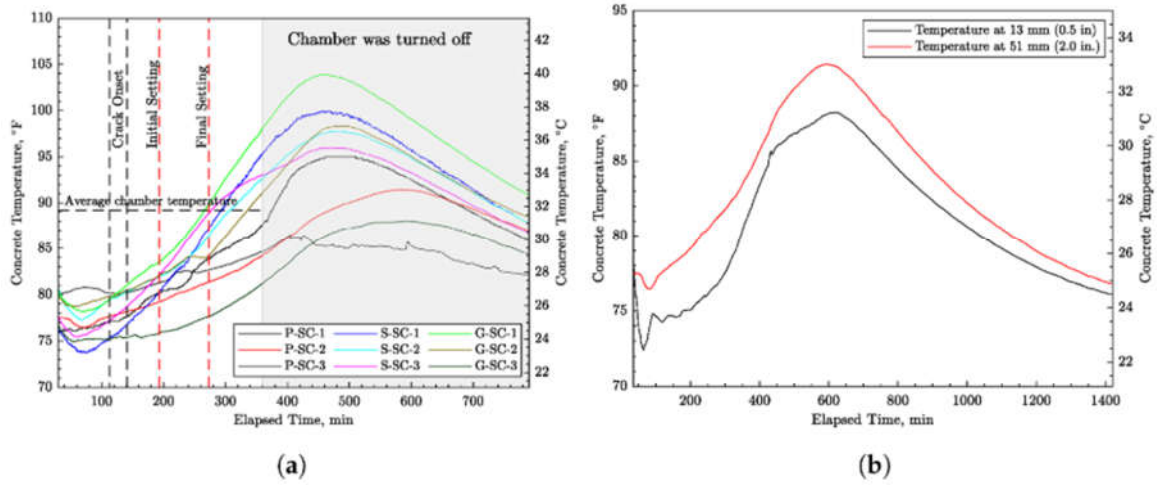

Figure 7. Concrete temperature development: (**a**) for all nine specimens at depth of 51 mm (2 in) and (**b**) at a different depth for specimen P-SC-2.

Figure 8 illustrates the estimated evaporation rates for all nine specimens, determined using Uno's equation [5] by incorporating measured values of concrete temperature, wind speed, ambient temperature, and relative humidity. The results indicate that evaporation rates are relatively low during the initial period following concrete placement. This reduced rate is partly associated with the early temperature evolution of the concrete, beginning around the time when cracking initiates. The shaded region in Figure 8 denotes the onset of strength gain as identified from the penetration resistance test results discussed later. Any increase in evaporation rate observed in certain specimens during this stage is not considered critical, since cracking had already occurred by that time.

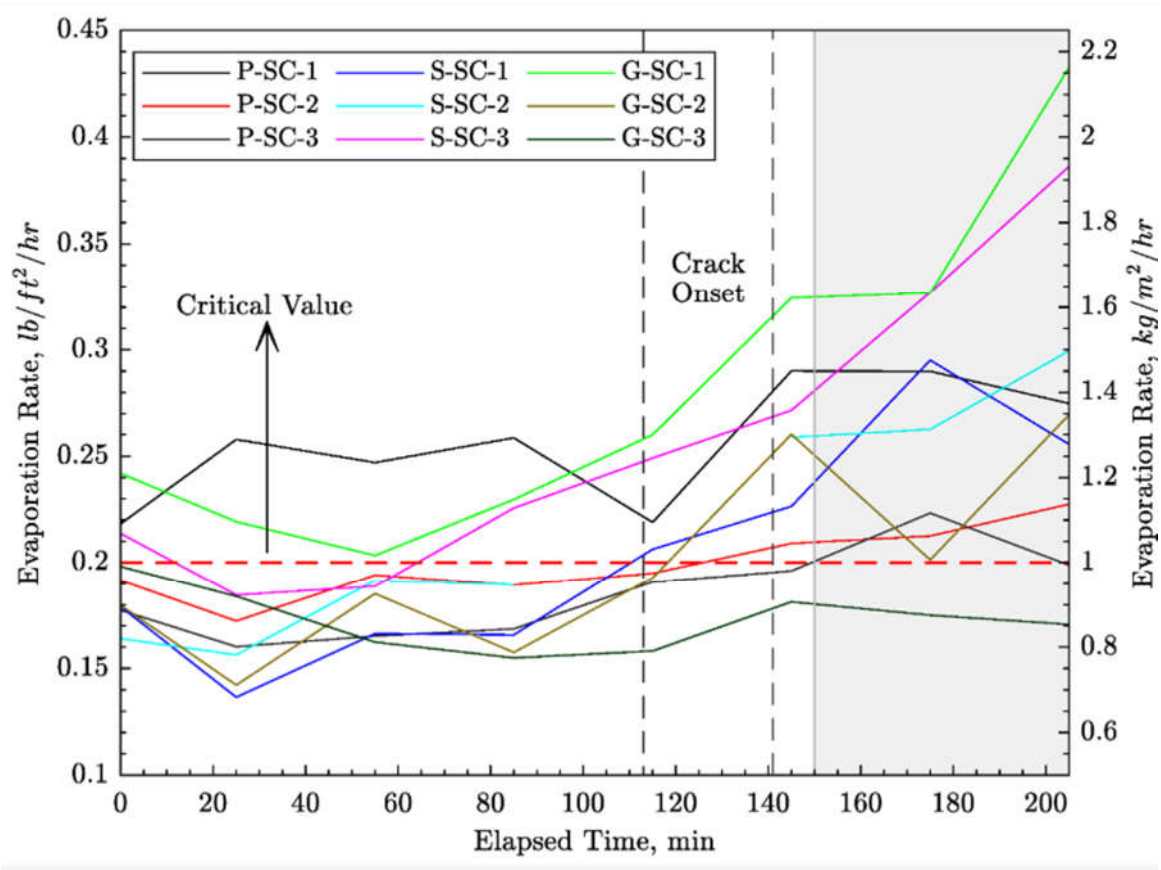

Figure 8. Estimated evaporation rate of water from the concrete surface.

Figure 9 illustrates the relationship between the measured crack widths and the corresponding average evaporation rates. For each specimen, the evaporation rate was averaged over the duration from casting to the onset of cracking. The results indicate that plastic shrinkage cracking may develop even when evaporation rates remain below the critical threshold of 1.0 kg/m²/h (0.2 lb/ft²/h) recommended in ACI 305R-20 [31]. Similar findings have also been reported in previous studies [24].

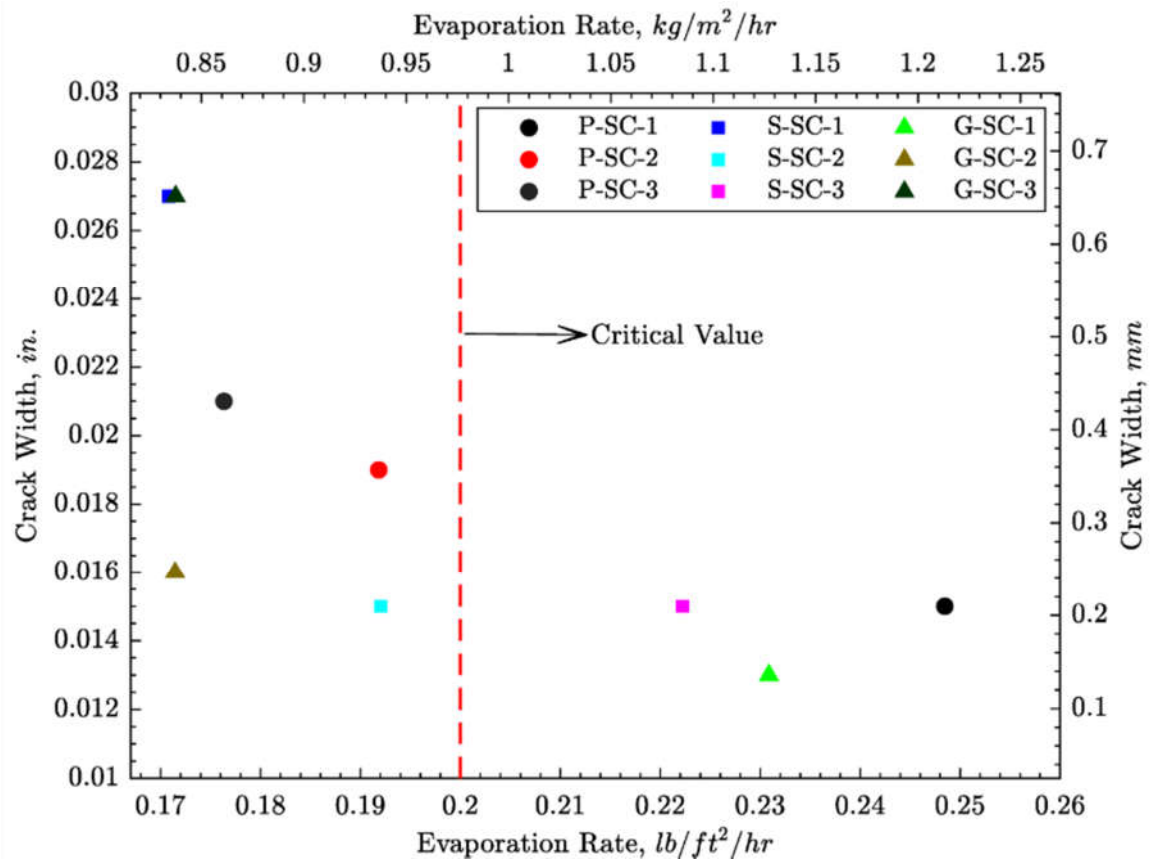

Figure 9. Measured crack width versus calculated evaporation rate.

Early-Age Bond Test

To explain the limited effectiveness of reinforcement in mitigating plastic shrinkage cracking observed during the shrinkage tests, early-age bond experiments were performed to assess the interaction between reinforcement and freshly placed concrete. The results indicate that the bond strength at approximately $t = 2$ h, which corresponds to the typical time of crack initiation, is only about 0.14 MPa. For reference, ASTM D7957-22 [32] specifies a minimum guaranteed bond strength of 7.6 MPa at 28 days of curing, defined as the mean bond strength minus three standard deviations. To prevent disturbance of the fresh concrete, the bond specimens were tested with the formwork left in place.

Figures 10 and 11 present the bond strength results for specimens reinforced with steel and GFRP bars. Steel reinforcement consistently exhibited higher bond strength than GFRP reinforcement after 1, 2, and 3 hours of exposure to the controlled environment. However, for both reinforcement types, the bond strength during the first 1 to 2 hours remained negligible, which coincides with the time frame in which plastic shrinkage cracking was observed. Moreover, a free-end slip of approximately 0.5 mm (0.02 in) was necessary to reach the maximum bond resistance, indicating that crack opening likely occurred before the development of peak bond strength.

To further evaluate the bond condition at the bar–concrete interface, the tested specimens were sectioned longitudinally after completion of the pullout tests. Representative examples are shown in Figure 12. The observed failure mode was characterized by direct bar pullout, with no evidence of radial cracking or localized damage around the reinforcement, confirming the weak bond at early ages.

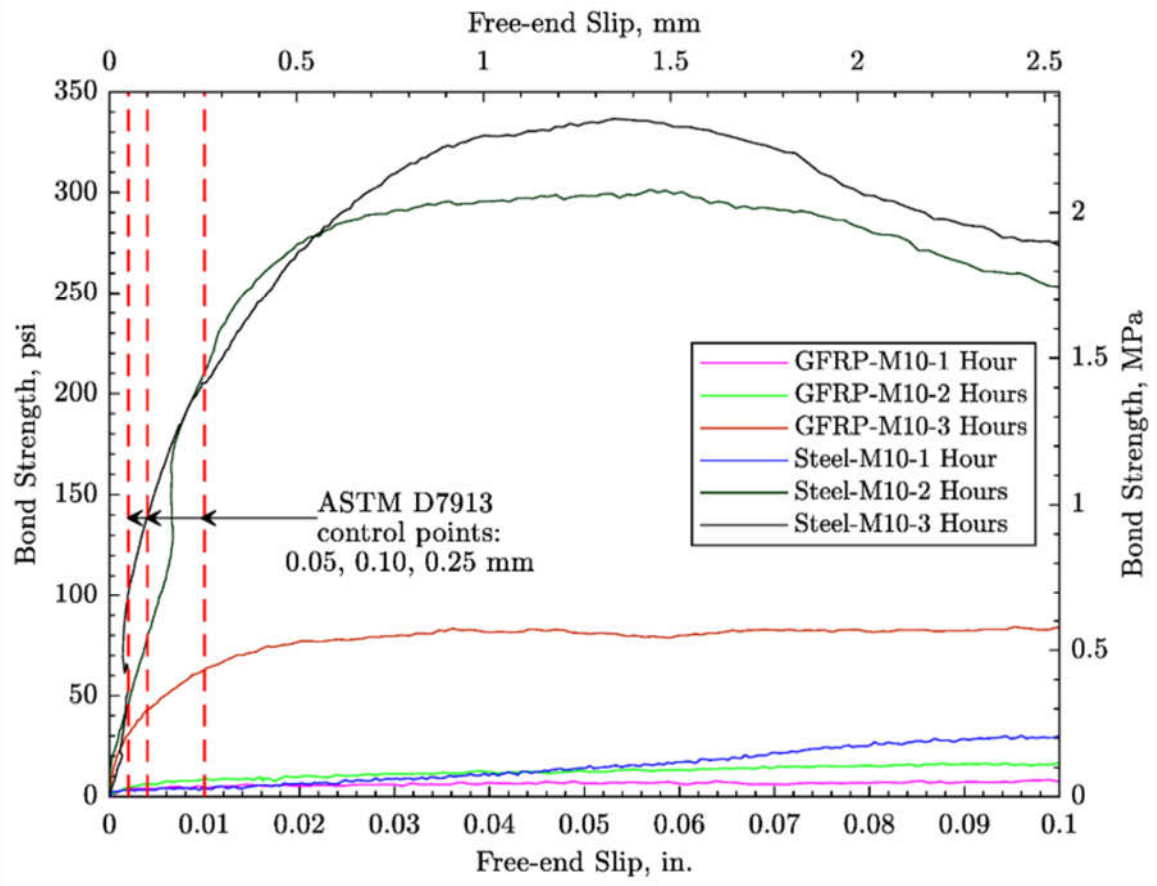

Figure 10. Bond stress–slip relationships.

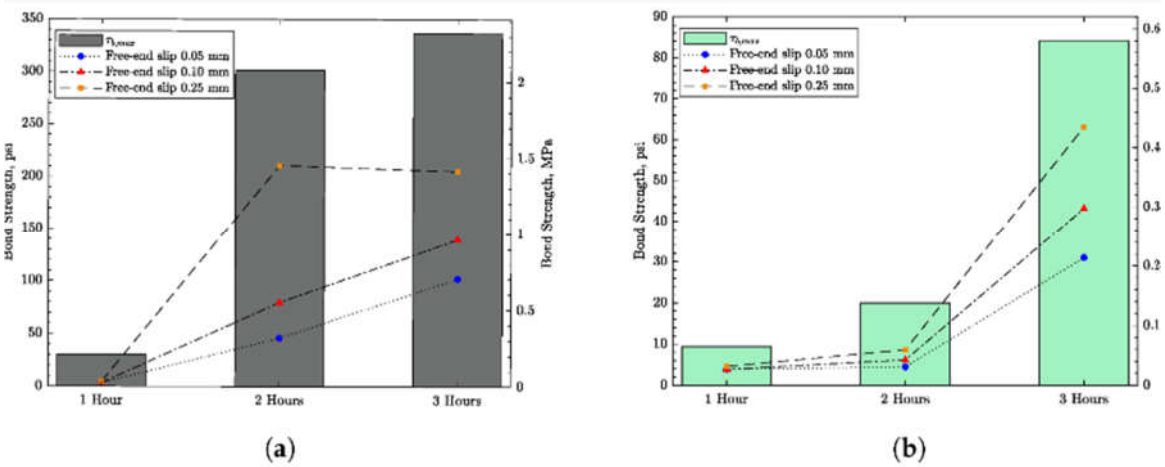

Figure 11. Pull-out test results: (**a**) steel reinforcement and (**b**) GFRP reinforcement.

Figure 12. Representative bond samples after failure: (**a**) Steel No. 3 at 1 h and (**b**) GFRP No. 3 at 1 h.

V. SIMULATION RESULTS AND DISCUSSION

Thermal Analyses

As an initial step, the degrees of hydration corresponding to the initial and final setting times, obtained from the penetration resistance tests, were further refined through numerical calibration. For this purpose, the 150 mm × 150 mm × 150 mm specimens were simulated using the VCLM framework while incorporating the relevant environmental boundary conditions. Because the concrete mixture was sieved to remove coarse aggregates, the effective cement content in the model increased to 687 kg/m³. By comparing the simulated degree-of-hydration curve with the penetration resistance measurements (Figure 13), the degree of hydration at initial setting was determined to be $\alpha_0 = 0.040$. This value aligns well with experimentally reported hydration levels at the onset of setting in cement pastes [62]. The degree of hydration corresponding to final setting was found to be $\alpha f = 0.089$.

For the thermal simulations of the slab specimens, the convective heat transfer coefficient was reduced by a factor of two-thirds. All remaining input parameters were defined based on the mixture proportions, experimentally recorded data—including wind speed, ambient temperature, and relative humidity—or values reported in the literature. Concrete temperatures were experimentally measured using thermocouples inserted through the plywood formwork into the concrete. To ensure direct comparability between numerical and experimental results, a computational node was placed at the exact location of the thermocouple tip in the numerical model.

Figure 14 compares the measured and simulated temperature histories starting from the time of casting for specimen S-SC-1, while additional comparisons for all specimens are also included. In this figure, simulated temperature curves are superimposed on the range of measured values. Specimens P-SC-2 and P-SC-3 were excluded from the experimental range due to their unusually low recorded temperatures and were therefore treated as outliers. Among all cases, specimen S-SC-1 exhibited the closest quantitative agreement between measured and simulated temperatures. Nevertheless, the numerical predictions captured the overall experimental trends satisfactorily across all specimens. Since the numerical models were identical in their formulation, the observed temperature differences arise solely from variations in environmental exposure and initial concrete temperature. The initial temperature reduction observed in most specimens was also reproduced in the simulations and was primarily attributed to evaporative cooling rather than other environmental influences.

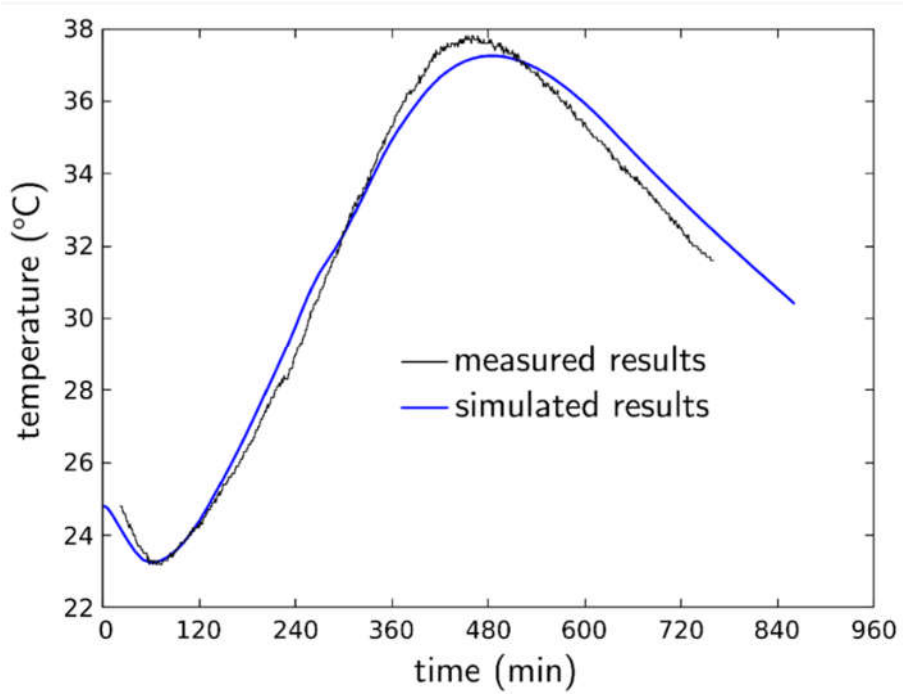

Figure 13. Physically measured and numerically simulated temperatures at the thermocouple location in specimen S-SC-1.

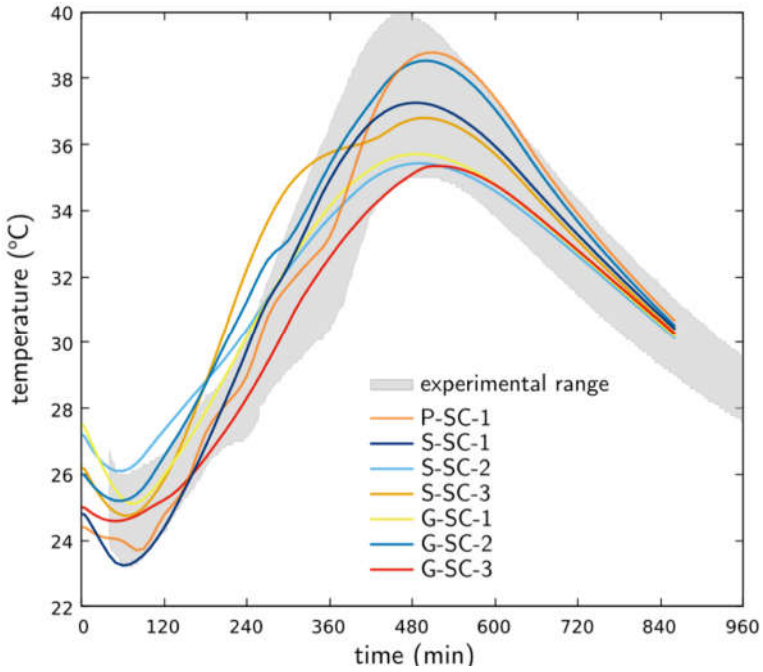

Figure 14. Numerically simulated temperatures for selected slab specimens. The experimentally measured range of temperature values is presented for comparison.

Cracking Behavior of Unreinforced Slab Specimens

To model the cracking response of the slab specimens, the previously developed thermal simulations were integrated with hygral and mechanical analysis modules [49]. In alignment with the experimental procedures, the interfaces between the concrete and the formwork were assumed to be frictionless. The measured ambient temperature, relative humidity, and wind velocity were applied as environmental boundary conditions throughout the simulations.

Before representing plastic shrinkage through volumetric strain, as illustrated in Figure 15, preliminary attempts were made to model plastic shrinkage as a diffusion-driven process similar to drying shrinkage. These efforts proved unsuccessful and conceptually inappropriate. The predicted crack widths at t = 6 h were significantly smaller than those measured experimentally. Additionally, widespread microcracking developed across the drying surface, and the resulting dominant crack initiated at the surface and propagated downward over the central restraint. In contrast, modeling plastic shrinkage as a volumetric strain produced a more realistic response, wherein the central restraint acted as a stress concentrator, leading to crack initiation at the device tip and upward propagation toward the surface. Similar upward crack propagation associated with plastic shrinkage has been documented by Ghourchian et al. [60] using X-ray radiography.

The numerical investigation included one representative specimen for each reinforcement configuration, namely P-SC-1, S-SC-1, and G-SC-1. Because the mechanical model requires finite stiffness and strength values to describe the cohesive behavior of concrete in its fresh state, and such properties are not readily available, the initial elastic modulus and tensile strength were assigned values of 0.002 $E(\alpha_u)$ and 0.02 $f(\alpha_u)$, respectively. These parameters were selected to reproduce cracking patterns consistent with experimental observations. Given that cracking occurs prior to final setting, the choice of these initial properties has a pronounced influence on the simulated response.

For specimen P-SC-1, which served as the unreinforced control case, cracking in the simulation initiated at approximately t = 130 min at the tip of the central restraining device. The crack subsequently propagated upward and became visible at the drying surface around t = 170 min. The simulated crack travel time from the device tip to the surface closely matches values reported from radiographic imaging studies [60]. Rapid crack propagation occurred during the phase of pronounced horizontal deformation shown in Figure 15. Consistent with experimental findings, cracking extended across the midspan of the specimen above the central riser (Figure 15). While discontinuous crack patterns observed in some laboratory specimens (Figure 5) were not reproduced numerically—likely due to the homogeneous nature of the material model—localized microcracking was predicted near the end restraints. Although not clearly visible in Figure 15, such behavior has also been reported in other experimental investigations [8].

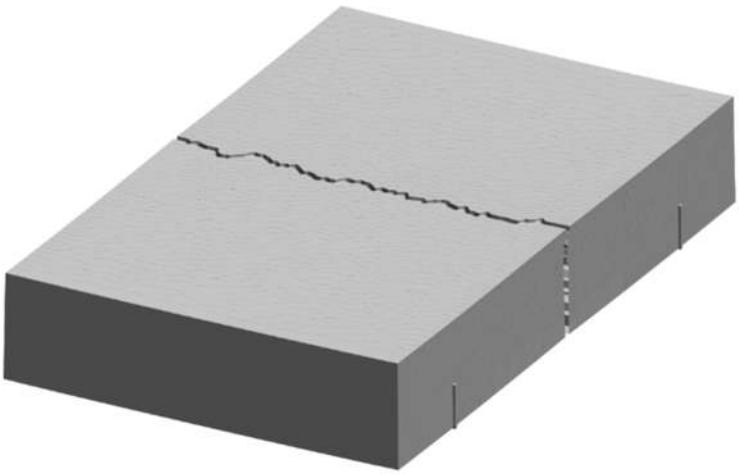

Figure 15. Numerically simulated crack pattern in specimen P-SC-1 at t = 6 h.

VI. CONCLUSIONS

This study combined experimental testing and numerical modeling to evaluate the effectiveness of GFRP bars in controlling early-age plastic shrinkage cracking in concrete slabs. Steel-reinforced and unreinforced specimens were also examined for comparison. Consistent cracking in control specimens was achieved by regulating mixture proportions, environmental conditions, and increasing the initial concrete temperature to enhance surface evaporation. Cracking occurred while the concrete was still in a plastic state.

The results indicate that neither GFRP nor steel reinforcement significantly delayed crack initiation or reduced crack width during plastic shrinkage. Crack openings remained relatively uniform across the slab

width, reflecting the limited bond development between reinforcement and concrete at early ages. Measured bond strengths at approximately 2 h were very low, which likely explains the ineffectiveness of bar reinforcement in restraining plastic shrinkage cracking.

Plastic shrinkage cracking was observed even at evaporation rates below the commonly cited critical value, highlighting the limitations of relying solely on evaporation criteria. Numerical simulations captured the key thermo-hygro-mechanical mechanisms governing early-age cracking and demonstrated that modeling plastic shrinkage as volumetric strain successfully reproduced observed crack initiation and propagation patterns.

Overall, the findings suggest that routinely spaced GFRP bar reinforcement is not effective in preventing plastic shrinkage cracking. For practical applications, distributed short fibers remain a more reliable solution for mitigating early-age cracking.

REFERENCES

References

1. Soroushian, P.; Mirza, F.; Alhozajiny, A. Plastic shrinkage cracking of polypropylene fiber reinforced concrete. *Mater. J.* **1993**, *92*, 553–560.
2. Otieno, M.; Alexander, M.; Beushausen, H.D. Corrosion in cracked and uncracked concrete—Influence of crack width, concrete quality and crack reopening. *Mag. Concr. Res.* **2010**, *62*, 393–404.
3. Kayondo, M.; Combrinck, R.; Boshoff, W. State-of-the-art review on plastic cracking of concrete. *Constr. Build. Mater.* **2019**, *225*, 886–899.
4. Wittmann, F. On the action of capillary pressure in fresh concrete. *Cem. Concr. Res.* **1976**, *6*, 49–56.
5. Uno, P.J. Plastic shrinkage cracking and evaporation formulas. *ACI Mater. J.* **1998**, *95*, 365–375.
6. Ravina, D.; Shalon, R. Plastic shrinkage cracking. *ACI J. Proc.* **1968**, *65*, 282–291.
7. Boshoff, W.P.; Combrinck, R. Modelling the severity of plastic shrinkage cracking in concrete. *Cem. Concr. Res.* **2013**, *48*, 34–39.
8. Combrinck, R.; Steyl, L.; Boshoff, W.P. Influence of concrete depth and surface finishing on the cracking of plastic concrete. *Constr. Build. Mater.* **2018**, *175*, 621–628.
9. Weiss, W.J. *Prediction of Early-Age Shrinkage Cracking in Concrete Elements*; Northwestern University: Evanston, IL, USA, 1999.
10. Ghoddousi, P.; Javid, A.A.S. Effect of reinforcement on plastic shrinkage and settlement of self-consolidating concrete as repair material. *Mater. Struct.* **2012**, *45*, 41–52.
11. Sule, M.; van Breugel, K. Cracking behaviour of reinforced concrete subjected to early-age shrinkage. *Mater. Struct.* **2001**, *34*, 284–292.
12. Design; CRC Press: Boca Raton, FL, USA, 2014.
13. Bank, L.C. Composites for Construction: Structural Design with FRP Materials; John Wiley & Sons: Hoboken, NJ, USA, 2006.
14. Taerwe, L.; Matthys, S. FRP for concrete construction: Activities in Europe. Concr. Int. **1999**, 21, 33–36
15. Fukuyama, H. FRP composites in Japan. Concr. Int. **1999**, 21, 29–32.